

Decoupling of static and dynamic criticality in a driven Mott insulator

Alberto de la Torre^{1,2}, Kyle L. Seyler^{1,2}, Michael Buchhold^{1,2}, Yuval Baum^{1,2}, Gufeng Zhang³, Nicholas J. Laurita¹, John W. Harter^{1,2}, Liuyan Zhao^{1,2}, Isabelle Phinney^{1,2}, Xiang Chen^{4,5}, Stephen D. Wilson⁵, Gang Cao⁶, Richard D. Averitt³, Gil Refael^{1,2} & David Hsieh^{1,2}✉

Strongly driven antiferromagnetic Mott insulators have the potential to exhibit exotic transient phenomena that are forbidden in thermal equilibrium. However, such far-from-equilibrium regimes, where conventional time-dependent Ginzburg-Landau descriptions fail, are experimentally challenging to prepare and to probe especially in solid state systems. Here we use a combination of time-resolved second harmonic optical polarimetry and coherent magnon spectroscopy to interrogate *n*-type photo-doping induced ultrafast magnetic order parameter dynamics in the antiferromagnetic Mott insulator Sr_2IrO_4 . We find signatures of an unusual far-from-equilibrium critical regime in which the divergences of the magnetic correlation length and relaxation time are decoupled. This violation of conventional thermal critical behavior arises from the interplay of photo-doping and non-thermal magnon population induced demagnetization effects. Our findings, embodied in a non-equilibrium phase diagram, provide a blueprint for engineering the out-of-equilibrium properties of quantum matter, with potential applications to terahertz spintronics technologies.

¹Department of Physics, California Institute of Technology, Pasadena, CA 91125, USA. ²Institute for Quantum Information and Matter, California Institute of Technology, Pasadena, CA 91125, USA. ³Department of Physics, University of California, San Diego, La Jolla, CA 92093, USA. ⁴Department of Physics, Boston College, Chestnut Hill, MA 02467, USA. ⁵Materials Department, University of California, Santa Barbara, CA 93106, USA. ⁶Department of Physics, University of Colorado, Boulder, CO 80309, USA. ✉email: dhsieh@caltech.edu

Dynamically driven interacting quantum many-body systems have the potential to exhibit properties that defy the laws of equilibrium statistical mechanics. A widely studied model is the impulsively driven antiferromagnetic (AFM) Mott insulator, which is predicted to realize exotic transient phenomena including dynamical phase transitions into thermally forbidden states^{1–3} and highly non-thermal magnon distributions⁴. The single-layer perovskite iridate Sr_2IrO_4 is a prototypical spin-orbit coupled AFM Mott insulator, serving as an ideal platform to explore such out-of-equilibrium behaviors. The low energy electronic structure of Sr_2IrO_4 consists of a completely filled band of spin-orbital entangled pseudospin $J_{\text{eff}} = 3/2$ states and a narrow half-filled band of $J_{\text{eff}} = 1/2$ states, which splits into lower and upper Hubbard bands due to on-site Coulomb repulsion⁵. Short-range AFM correlations between $J_{\text{eff}} = 1/2$ moments within a layer are established well above room temperature^{6,7}. But owing to weak interlayer exchange coupling ($J_c < 10^{-3} J_{ab}$)^{7,8}, three-dimensional (3D) long-range AFM ordering only occurs below a Néel temperature $T_N = 230$ K. The ordered structure exhibits a weak in-plane ferromagnetic moment in each layer due to pseudospin canting, which is staggered along the c -axis (Fig. 1a). Resonant x-ray and neutron scattering measurements of La-doped Sr_2IrO_4 have shown that a small concentration of n -type carriers destroys c -axis ordering, leaving behind a paramagnetic state with short-range 2D AFM correlations^{9–11}. As such, n -type photo-doping, which may be simulated by optically pumping electrons from the electronically inert $J_{\text{eff}} = 3/2$ band into the upper Hubbard band, provides a potential pathway to impulsively quench long-range AFM order.

Recently, both ultrafast optical and free-electron laser-based resonant x-ray scattering (RXS) methods have been used to probe photo-doping induced pseudospin dynamics in iridates^{12–16}. In the case of Sr_2IrO_4 , one study showed that it could be made magneto-optically active by aligning the canted moments in an external magnetic field¹⁴. Transient magnetization dynamics were then probed in the near-equilibrium weak photo-doping limit using time-resolved magneto-optical Kerr effect (MOKE) spectroscopy. The recovery time of the net magnetization was observed to diverge at T_N , which was explained within a time-dependent Ginzburg–Landau framework. In another pair of studies, time-resolved RXS was used to probe long-range AFM order parameter dynamics without a field in a far-from-equilibrium strong photo-doping regime^{12,13}. A non-thermal melting of the AFM order was achieved, but no critical dynamics were resolved across this phase transition.

The behavior of a system near a dynamical phase boundary should be sensitive to small changes in excitation density. In order to resolve out-of-equilibrium critical dynamics, it is therefore imperative that the excitation density be uniform throughout the probed volume and finely sampled near the phase boundary. Since the pump excitation density invariably decays with depth into the sample, one should in principle probe exclusively within a small interval of depth to minimize the effects of averaging over different excitation densities, which might otherwise obscure features of criticality (Supplementary Notes 1 and 2).

Here we meet this condition by using time-resolved second harmonic generation rotational anisotropy (SHG-RA). In combination with time-resolved MOKE, we probe the transient suppression and recovery of long-range magnetic order in Sr_2IrO_4 induced by n -type photo-doping. We report signatures of an unusual far-from-equilibrium critical regime in which the divergences of the magnetic correlation length and relaxation time are decoupled.

Results

Pump-induced instantaneous SHG response. The SHG-RA technique (Fig. 1b) was recently shown to be directly sensitive to the magnetization of the topmost layer of Sr_2IrO_4 in zero

magnetic field^{17,18}. We note that while an additional hidden order has been reported in Sr_2IrO_4 ^{19,20}, there is no indication that SHG couples to any hidden order¹⁸, contrary to a previous interpretation²¹. In an SHG-RA experiment, light is focused obliquely onto the (001) face of Sr_2IrO_4 and the intensity of light reflected at twice the incident frequency $I(2\omega)$ is measured as the scattering plane is rotated about the surface normal. In equilibrium, SHG-RA patterns acquired above T_N exhibit four-fold (C_4) rotational symmetry, arising from bulk electric-quadrupole (EQ) radiation from its centrosymmetric crystallographic point group¹⁸. Below T_N , an additional surface magnetization-induced electric-dipole (SMIED) contribution turns on and interferes with the EQ contribution, lowering the symmetry of the SHG-RA pattern from C_4 to C_1 (Fig. 1c).

To study the effects of n -type photo-doping, we developed time-resolved pump-probe SHG-RA using the apparatus depicted in Fig. 1b. The pump beam, which was tuned on resonance with the $J_{\text{eff}} = 3/2$ band to upper Hubbard band transition, and probe beam were focused within a single magnetic domain for our experiments. Figure 1d shows transient SHG-RA data acquired at the instant of pump excitation ($t = 0$) as a function of pump fluence (F). In the un-pumped case ($F = 0$), the C_1 symmetry of the SHG-RA pattern is manifested through the presence of a dominant intensity lobe, indicating a finite SMIED contribution and thus a finite magnetic order parameter. As F increases, the intensity of the dominant lobe decreases linearly until it plateaus above a critical fluence $F_c \approx 0.9$ mJ/cm². Beyond F_c , the non-magnetic C_4 symmetry is fully restored to the SHG-RA pattern, signaling a collapsed SMIED contribution. The slightly higher C_4 -EQ yield from the pump-induced compared to heating-induced non-magnetic state likely arises from un-relaxed bulk magneto-elastic deformations that will be discussed in more detail below. The prompt change in the SHG-RA pattern within the time resolution of our instrument (<200 fs) for all fluences is consistent with a photo-doping scenario. Specifically, AFM order is suppressed by magnetic defects that are left in the wake of propagating doublons (Fig. 1b), which are generated on the timescale of the nearest-neighbor hopping (<20 fs)^{14,22,23}. Moreover, the observed critical fluence corresponds to an excitation density (n_{ex}) of approximately 0.05 per iridium site, which is close to the reported critical La-doping level to suppress AFM order^{9,10}, suggestive of an optical n -type doping induced quench mechanism.

More detailed comparisons between the properties of Sr_2IrO_4 in and out-of-equilibrium can be made by mapping the fluence versus temperature magnetic phase diagram. This is accomplished by collecting an array of SHG-RA patterns immediately after optical excitation across different starting temperatures and pump fluences and then tracking the onset of the SMIED contribution. For $F = 0$, the SMIED contribution emerges below T_N as expected (Fig. 2a). With increasing F , this transition shifts monotonically to lower temperatures, indicating that F_c increases upon cooling. By plotting T_N as a function of n_{ex} , or equivalently F_c as a function of T , a sharp out-of-equilibrium magnetic phase boundary is identified. Despite an instantaneous electronic temperature that already far exceeds T_N at $F \approx 0.2$ mJ/cm² based on the electronic specific heat of Sr_2IrO_4 (see Supplementary Note 3), the photo-doping and La-doping phase boundaries nearly coincide over the small La-doping range where AFM order exists in equilibrium^{9,10} (Fig. 2b). This indicates that heat transfer from the charge to pseudospin subsystem is negligible near $t = 0$. Since chemical doping differs from photo-doping in non-trivial ways, including the introduction of a disorder that is known to nucleate non-magnetic metallic puddles in La-doped Sr_2IrO_4 ^{9,24}, we refrain from drawing more detailed comparisons.

At later time delays, the charge, pseudospin, and lattice subsystems are typically expected to thermalize and thus the out-

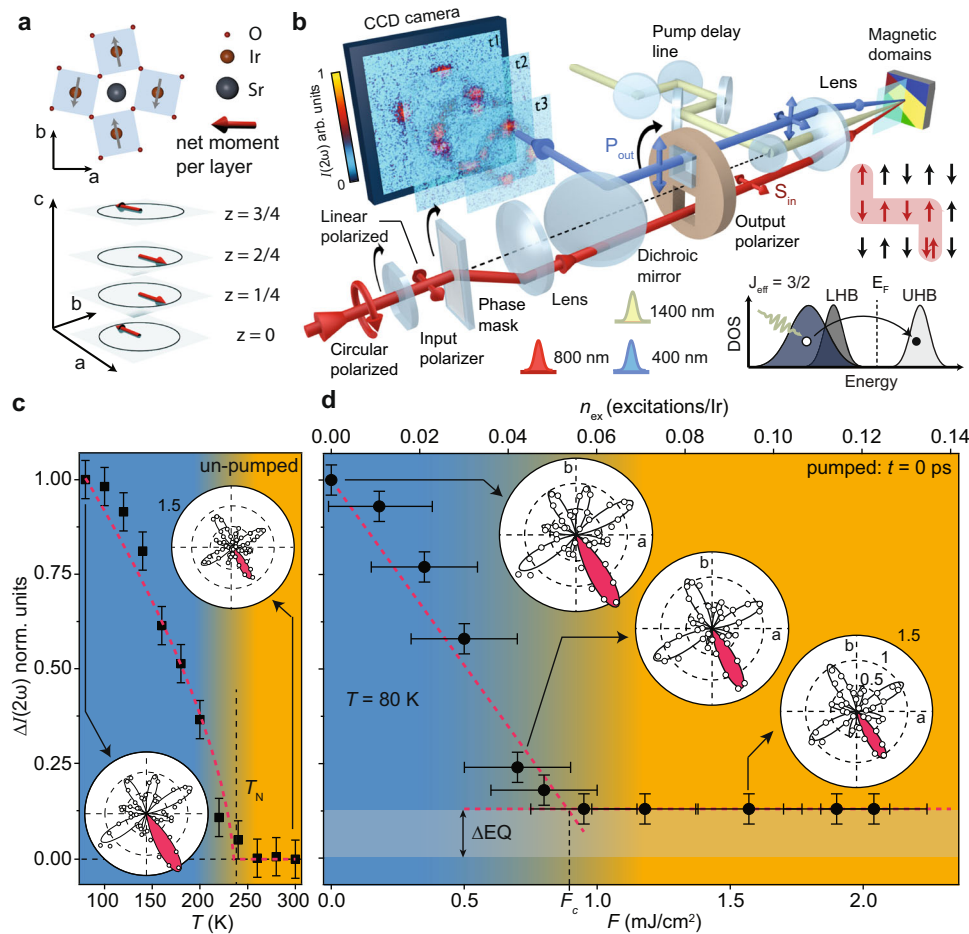


Fig. 1 Instantaneous photo-doping response of magnetic order in Sr₂IrO₄. **a** Schematic of an IrO₂ layer (O: red; Ir: orange; Sr: gray spheres). Azule squares represent the *ab*-plane projection of the IrO₆ octahedra and gray arrows represent the $J_{\text{eff}} = 1/2$ pseudospins. Each IrO₂ layer, shown as blue planes at $z = 0, 1/4, 2/4, 3/4$, with z the fractional coordinate along the c -axis, possesses a net moment (red arrow) due to pseudospin canting, which is staggered along the c -axis. **b** Schematic of the time-resolved second harmonic generation rotational anisotropy (SHG-RA) setup (See “Time-resolved spectroscopic probes”). Wavelengths of the pump pulse and incident and SHG probe pulses are color-coded. Curved black arrows indicate co-rotating optical elements. Data shown throughout the manuscript are acquired in the $P_{\text{in}}\text{-}S_{\text{out}}$ polarization channel. Different colors on the sample represent distinct magnetic domains. Inset: schematic of n -type photo-doping and resulting doublon generation and propagation through the antiferromagnetic lattice (red line). DOS density of states, LHB (UHB) lower (upper) Hubbard band, E_F Fermi energy. **c** Temperature dependence of the change in SHG intensity $\Delta I(2\omega)$ relative to $T = 300$ K for an un-pumped sample acquired at the angle of maximum intensity (red shaded lobe in the SHG-RA plots). The red dashed line is a guide to the eye and the vertical dashed line marks the Néel temperature (T_N). Vertical error bars represent the range of intensity values obtained upon selecting different regions of the CCD camera for radial integration and background subtraction in order to convert raw data into SHG-RA intensity patterns. **d** Pump fluence dependence of $\Delta I(2\omega)$ at $t = 0$ and $T = 80$ K with corresponding SHG-RA patterns (white circles). Fits to the data below (above) F_c including both electric-quadrupole (EQ) and surface magnetization-induced electric-dipole (SMIED) terms (solely EQ term) are overlaid (black lines). Height of the gray bar represents the change in EQ SHG intensity with respect to the equilibrium value as discussed in the main text. Horizontal error bars represent an upper bound on the uncertainty in the calculation of n_{ex} assuming $F = 2$ mJ/cm² (as described in “Conversion from F to n_{ex} ”). The SHG-RA intensities are normalized to the $T = 300$ K value (circular grid scale).

of-equilibrium phase diagrams mapped at $t \approx 0$ and $t \gg 0$ should be different. Figure 2c shows the intensity of the dominant SHG-RA lobe over a range of fluence values, converted into effective temperatures using the total specific heat of Sr₂IrO₄ (see Supplementary Note 3), acquired at $t = 10$ ps, which far exceeds the reported charge and lattice relaxation timescales but is much shorter than the timescale for heat to escape the probed region^{23,25}. At low fluences, we find excellent agreement with the un-pumped temperature dependence data, confirming a pure optical heating effect. Surprisingly however, there is increasing bifurcation of the curves above $F \approx 0.8$ mJ/cm², leading to a growing mismatch between the out-of-equilibrium phase boundary mapped at $t = 10$ ps and that calculated assuming pure optical heating as a function of fluence (Fig. 2d). This indicates that

thermalization of the pseudospin subsystem is impeded at high fluences.

A hallmark of the La-doping induced paramagnetic state is the persistence of short-range intralayer AFM correlations, manifested through remnant dispersive 2D magnons detected by resonant inelastic x-ray scattering^{10,11}. To search for similar intralayer correlations in the photo-induced paramagnetic phase of Sr₂IrO₄, we leverage the fact that the zone center 2D magnon mode with B_{2g} symmetry is weakly gapped (≈ 2 meV) and Raman active^{26,27}. This allows the magnon to be coherently excited by our pump pulse via impulsive stimulated Raman scattering and optically tracked in the time domain using ultrafast MOKE spectroscopy²⁸. Figure 2e, f show typical SHG and MOKE transients acquired in the high pump fluence ($F \gg F_c$) regime.

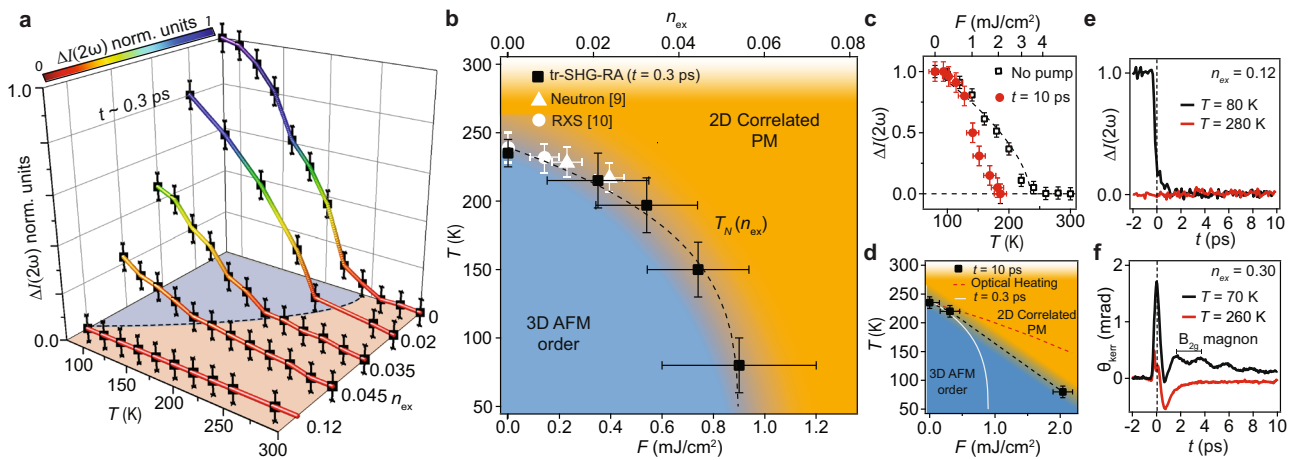


Fig. 2 Out-of-equilibrium magnetic phase diagrams. **a** Temperature dependence of the change in second harmonic generation (SHG) intensity $\Delta I(2\omega)$ at $t = 0.3$ ps, normalized to the un-pumped value at $T = 80$ K, for select pump excitation densities n_{ex} . **b** Out-of-equilibrium phase diagram mapped at $t = 0.3$ ps by either sweeping T or n_{ex} . Black squares mark the temperature onset of the surface magnetization-induced electric-dipole (SMIED) contribution at different fluences, $T_N(n_{ex})$. Dashed curve and blue-orange background are guides to the eye. The reported La-doping dependence of T_N is overlaid. **c** Comparison of the temperature dependence of $\Delta I(2\omega)$ for an un-pumped sample with the fluence (F) dependence of $\Delta I(2\omega)$ collected at $t = 10$ ps and $T = 80$ K, where F is converted into an effective temperature by assuming all of the pump energy goes into quasi-equilibrium heating. Dashed curve is a guide to the eye. **d** Out-of-equilibrium phase diagram mapped at $t = 10$ ps (black squares). Dashed black line and blue-orange background are guides to the eye. Overlaid are the phase boundary reproduced from panel **b** (white line) and that calculated assuming all of the pump energy goes into quasi-equilibrium heating (red line). **e** High fluence $\Delta I(2\omega)$ and **f** magneto-optical Kerr effect transients acquired below and above T_N . Vertical error bars in panels **a**, **c** represent the range of intensity values obtained upon selecting different regions of the CCD camera for radial integration and background subtraction in order to convert raw data into SHG-RA intensity patterns. Horizontal error bars in panels **c**, **d** represent the uncertainty in fluence due to laser drift. Horizontal (vertical) error bars in panel **b** (panels **b**, **d**) represent the uncertainty in our estimate of the critical n_{ex} ($T_N(n_{ex})$).

Despite a complete collapse of the magnetic order parameter over the displayed 10 ps time window (Fig. 2e) as evidenced by an absence of any SMIED contribution, coherent oscillations of the infinite wavelength B_{2g} magnon continue to be supported (Fig. 2f). This provides clear evidence of a significant 2D magnetic correlation length in the transient paramagnetic state, suggesting a non-thermal analog of La-doped Sr_2IrO_4 is realized. These results are consistent with and complementary to a time-resolved RXS study of Sr_2IrO_4 ¹², which showed that photo-doping strongly suppresses an AFM Bragg peak but does not alter the main high energy and short-wavelength features of the intralayer magnon spectrum (see Supplementary Note 4).

Temporal evolution of the SHG response. Having comprehensively mapped the transient magnetic phase diagram of Sr_2IrO_4 , we now finely examine the out-of-equilibrium critical dynamics. Figure 3a, b show the time-dependent change in intensity $\Delta I(2\omega)$ of the dominant SHG-RA lobe acquired at $T = 80$ K over a range of pump fluences. For $F \ll F_c$ (Fig. 3a), we observe a rapid drop in $\Delta I(2\omega)$ at $t = 0$ signifying a reduction of the SMIED contribution. This is followed by an exponential recovery with rise time $\tau \approx 1$ –2 ps towards a value negatively offset from the $t < 0$ intensity, which we showed (Fig. 2c, d) represents a thermalized state with a slightly elevated temperature. As F increases, τ rises slightly but exhibits no discontinuity at F_c despite the SMIED contribution vanishing. However, as F exceeds F_c , the point where C_4 symmetry is restored, τ continues to grow and eventually diverges around $F^* \approx 1.6$ mJ/cm² (Fig. 3b, c). Similar dynamics are observed if instead F is kept fixed and T is varied (inset Fig. 3a). These data reveal that the divergence of the magnetic correlation length and relaxation time occur along separated critical lines in the out-of-equilibrium phase diagram marked by F_c and F^* respectively (inset Fig. 3c). Such a decoupling is forbidden in equilibrium and is also not observed across dynamical phase transitions in weakly correlated ferromagnets²⁹ and charge density wave systems³⁰.

We note the presence of a subtle exponential drop just after $t = 0$ that becomes more pronounced at large F . This causes $\Delta I(2\omega)$ to drop below the instantaneous EQ value (gray bar in Figs. 1 and 3a, b) and ultimately plateau at the high-temperature EQ value upon reaching F^* . Given that magneto-elastic deformations are known to occur below T_N in Sr_2IrO_4 ⁸ and can cause small changes in the EQ response, a possible origin of this exponential component is lattice relaxation following impulsive suppression of the magnetic order parameter. Therefore, only at large F when τ sufficiently exceeds the relevant phonon timescales do the magneto-elastic deformations have time to fully relax (see Supplementary Note 5).

Discussion

To check whether the divergence of τ simply results from a prolonged photo-dopant lifetime, we performed simultaneous transient linear reflectivity ($\Delta R/R$) and SHG-RA measurements below T_N to directly compare the charge and pseudospin dynamics. As shown in Fig. 4a–c, the generation of photo-dopants and their subsequent suppression of the SMIED contribution both occur within the time resolution of our experiment. However, unlike the SHG response, we observe no saturation in the amplitude of $\Delta R/R$ and no significant change in its characteristic recovery time ($\tau_0 \approx 1$ ps) as a function of fluence (inset Fig. 4a), demonstrating that the slow dynamics observed at F^* occur exclusively in the pseudospin sector. This suggests that τ must be governed by the relaxation of excess magnons that are emitted upon doublon decay. One possibility is that the magnons rapidly thermalize to a higher temperature and that τ represents the timescale for the hot pseudospin subsystem to cool via heat exchange with the lattice and charge subsystems. However, a three-temperature model describing this process predicts that magnons should cool faster at higher excitation densities. Moreover, it fails to produce any diverging timescale (Supplementary Notes 3 and 6). This points to the alternative possibility

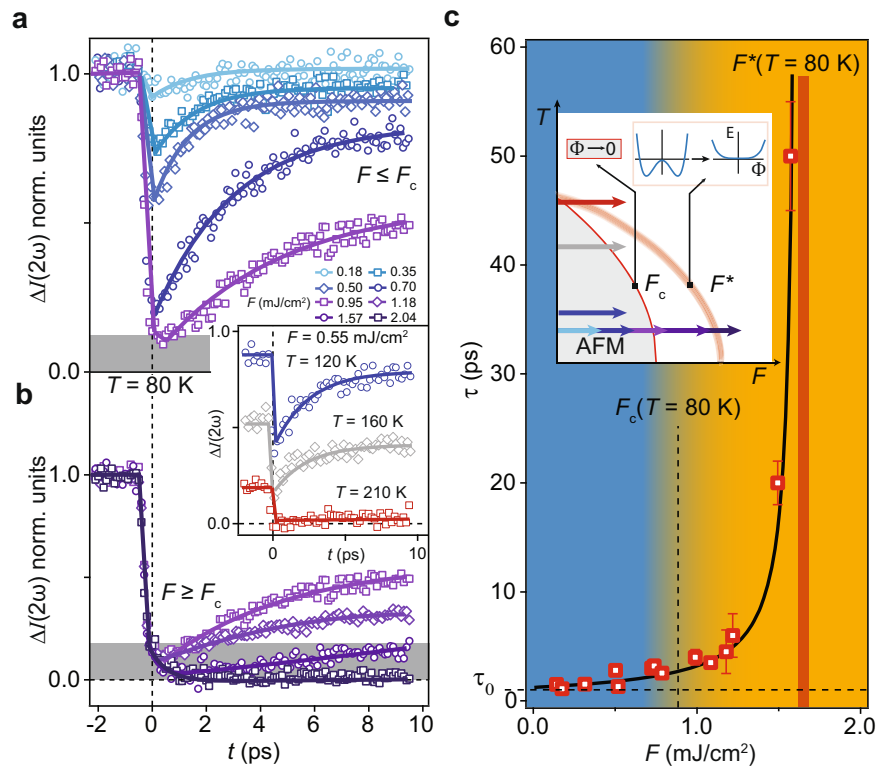


Fig. 3 Out-of-equilibrium critical dynamics of the magnetic order parameter. Transient change in second harmonic generation (SHG) intensity $\Delta/(2\omega)$ acquired at $T = 80$ K for select fluences (F) **a** below and **b** above the critical fluence F_c . The height of the gray bar denotes the excess electric-quadrupole (EQ) SHG intensity at $t = 0$ as discussed in the Results section “Temporal evolution of the SHG response”. Inset shows analogous data acquired at fixed $F = 0.55$ mJ/cm² for different temperatures. Solid lines are fits of the recovery to a single exponential function plus a constant determined by the long time offset of the SHG intensity. **c** Plot of fitted exponential relaxation times, τ , versus fluence superposed with a fit to the function $\tau = \tau_0(1 - F/F^*)^{-1}$, with τ_0 fixed to 1.2 ps as described in the Discussion section. The values of F_c (dashed vertical line and blue-orange background) and F^* (orange vertical bar) at $T = 80$ K based on the data in panels **a**, **b** and the fit (black line) respectively are explicitly marked. The decoupling of the divergence in magnetic correlation length (defined by F_c) from the divergence in relaxation time (defined by F^*) is illustrated in the inset based on the data in panels **a** and **b**. The arrows are color-coded in correspondence to the curves in panels **a** and **b** and point to the location in the out-of-equilibrium phase diagram being accessed. Schematics show the out-of-equilibrium free energy landscape after doublon decay based on the Langevin theory described in the text. Vertical error bars represent the uncertainty in τ obtained from fits to the exponential function shown in panels **a**, **b**.

that τ represents the timescale for the pseudospin subsystem to internally thermalize.

The rate-limiting step for recovering long-range magnetic order is the establishment of c -axis correlations (Fig. 2e, f). Therefore τ must be set by the thermalization time of interlayer c -axis magnons. However, the large mismatch between J_c (≈ 10 μ eV)^{7,8} and both the charge gap (≈ 250 meV)³¹ and lowest optical phonon energy (≈ 10 meV)²⁷ of Sr_2IrO_4 should impede c -axis magnon thermalization via charge or phonon excitation processes, leaving magnon–magnon scattering as the dominant thermalization channel. Building on the seminal work of Hohenberg and Halperin³², we study the critical dynamics after doublon decay of this effectively closed c -axis magnon subsystem via a general stochastic Langevin equation for a real order parameter in one spatial dimension (Supplementary Note 7):

$$\partial_t \varphi_k(t) = -\left(k^2 + \tau_0^{-1}\right) \varphi_k(t) - \lambda \int \frac{dk_1}{2\pi} \int \frac{dk_2}{2\pi} \varphi_{k_1}(t) \varphi_{k_2}(t) \varphi_{k-k_1-k_2}(t) + \xi_k(t) \quad (1)$$

where $\varphi_k(t)$ is the k -th Fourier component of the magnetic order parameter field $\varphi(z, t)$ that parameterizes the ordering of the intralayer Néel vector along the c -axis (Fig. 4d, e), τ_0^{-1} is a temperature-dependent mass term that is equivalent to the thermalization rate in a linearized Boltzmann equation³³, and λ parameterizes the interaction between magnons. Going beyond

conventional time-dependent Ginzburg–Landau descriptions, we introduce a Gaussian noise term $\xi_k(t)$ with $\langle \xi_k(t) \xi_{k'}(t') \rangle = \delta(t - t') \delta(k + k') (k^2 + \tau_0^{-1}) [2n_k(t) + 1]$ that imprints a non-equilibrium fluctuation-dissipation relation for some general magnon distribution function $n_k(t)$, in which the modes transverse to the c -axis are assumed to relax much faster and are thus integrated out³⁴. To leading order, the equation of motion for the magnetic order parameter $\Phi(t) = \langle \varphi_{k=0}(t) \rangle$ is given by $\partial_t \Phi(t) = -\tau^{-1} \Phi(t) - \lambda \Phi(t)^3$, and the Boltzmann equation for the magnon distribution is given by $\partial_t n_k(t) = -\tau^{-1} [n_k(t) - n_k^T]$, where $\tau^{-1} = \tau_0^{-1} - \lambda N_{\text{mag}}$ and n_k^T is the Bose distribution function corresponding to the final equilibrated magnon temperature T . These equations show that, in a closed system, the rate at which the magnetic order parameter recovers to its equilibrium value at T via magnon thermalization is a decreasing function of the total number of excited magnons (N_{mag}). This provides an explanation for all key features of the data in Fig. 3c. In the low pump fluence limit where $N_{\text{mag}} \ll 1/\tau_0 \lambda$, τ approaches a lower bound that is naturally set by the photo-dopant decay time τ_0 . As N_{mag} grows with fluence, τ exhibits a power-law increase following the reduced curvature of the Mexican hat potential. Finally once N_{mag} reaches $1/\tau_0 \lambda$ at the critical fluence F^* , τ diverges even though the total energy of the magnetic subsystem remains sub-critical (see Supplementary Note 7). For $F \geq F^*$, thermalization

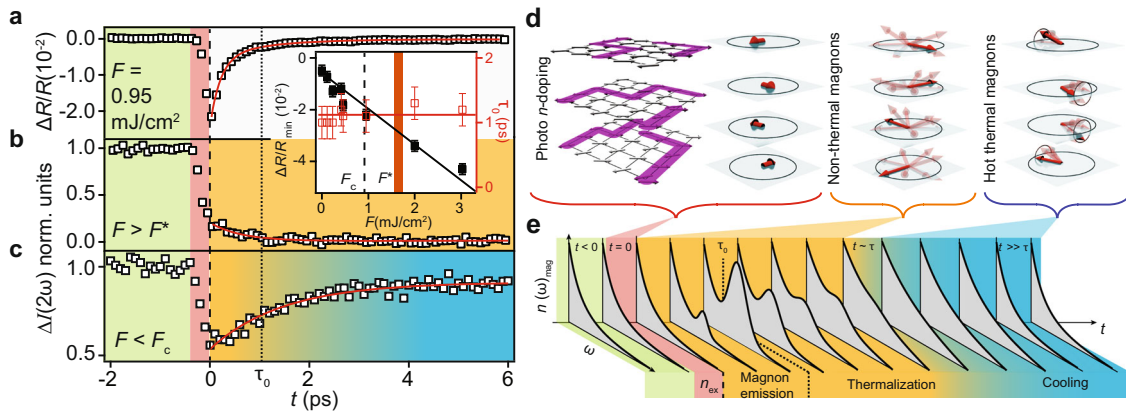


Fig. 4 Magnon population induced critical slowing down. Simultaneous measurements of the **a** transient reflectivity $\Delta R/R$ and **b, c** transient change in second harmonic generation (SHG) intensity $\Delta I(2\omega)$ acquired under identical experimental conditions (except for fluence) at $T = 80$ K. Inset of panel **a**: fluence dependence of the $\Delta R/R$ minimum (black markers) and characteristic recovery time τ_0 (red markers) extracted through double exponential fits (red curve) to the $\Delta R/R$ data (See “Exponential fitting procedure for linear reflectivity”). Red vertical error bars represent the uncertainty in τ_0 obtained from fitting to the double exponential function. Black error bars represent the standard deviation of the $\Delta R/R$ minimum over six independent measurements. Solid lines are guides to the eye. The dashed line and orange bar mark the critical fluence, F_c , and the fluence at which the relaxation time diverges, F^* , respectively. **d** Schematic of the complete temporal evolution of the real space *c*-axis magnetic correlations. The generation and propagation of doublons (purple lines) induce a suppression of long-range antiferromagnetic order as illustrated by a reduction of the net moment (red arrows; circle represents the equilibrium value) and a decoupling between layers (blue planes). Moment fluctuations occurring at later stages in time are captured by semi-transparent red arrows. **e** Schematic of the temporal evolution of the magnon distribution function $n(\omega)$ versus energy ω following pump excitation. Background colors denote different stages of temporal evolution as labeled in the figure. Over the time window $0 < t \leq \tau$ (shaded orange), $n(\omega)$ departs from Bose-Einstein form.

can still eventually occur through the weak coupling between *c*-axis magnons and phonons, which is likely responsible for the slow (>100 ps) recovery of the magnetic order parameter observed by time-resolved RXS measurements at high fluences^{12,13}. Ultimately, on even longer timescales, the system cools back to the initial temperature via heat diffusion out of the pumped region (Fig. 4d, e).

Conclusions

Altogether, our results provide experimental signatures that static and dynamic critical behavior can be decoupled in a Mott antiferromagnet upon driving due to a subtle interplay of photo-doping and magnon thermalization processes (Fig. 4d, e). The hierarchy of magnetic, phononic and charge gap energy scales that enables this behavior in Sr_2IrO_4 is typical for layered transition metal oxide based AFM Mott insulators including the high- T_c superconducting cuprates, suggesting that our reported phenomena may be operational in numerous layered quantum materials. This raises the intriguing prospect of fine-tuning parameters such as τ_0 , F_c , and F^* to optimize desired out-of-equilibrium properties. For example, extending τ_0 may be a pathway for realizing metastable electronic instabilities in a photo-doped Mott insulator, while the combination of a small τ_0 and F_c with a large F^* would be favorable for low-power high-speed AFM switching applications.

Methods

Sample growth. Single crystals of Sr_2IrO_4 were grown using a self-flux technique from off-stoichiometric quantities of IrO_2 , SrCO_3 , and SrCl_2 . The ground mixtures of powders were melted at 1470°C in partially capped platinum crucibles. The soaking phase of the synthesis lasted for >20 h and was followed by a slow cooling at $2^\circ\text{C}/\text{h}$ to reach 1400°C . From this point, the crucible is brought to room temperature through rapid cooling at a rate of $100^\circ\text{C}/\text{h}$. Crystals were cleaved along the (001) face just prior to measurements and immediately pumped down to a pressure $< 5 \times 10^{-6}$ torr in an optical cryostat.

Time-resolved spectroscopic probes

Time-resolved SHG-RA. Experiments were performed by splitting light from a regeneratively amplified Ti:sapphire laser, which produces 100 fs pulses with central wavelength $\lambda = 800$ nm at a repetition rate of 100 kHz, into pump and probe

arms. The pump beam feeds an optical parametric amplifier, whose 1400 nm output beam is linearly polarized and sent through a delay line before being focused at normal incidence onto a $90\ \mu\text{m}$ spot (FWHM) located within a single magnetic domain of a Sr_2IrO_4 crystal. As shown in Fig. 1b, the circularly polarized probe laser pulse ($\lambda = 800$ nm) traverses a linear input polarizer, phase mask, and collimating lens and is focused at oblique incidence ($\approx 10^\circ$) onto a $30\ \mu\text{m}$ spot within the pumped sample area using an objective lens. The reflected SHG pulse ($\lambda = 400$ nm) is re-collimated by the objective lens, linearly polarized by an output polarizer and then deflected onto a CCD camera by a triad of dichroic mirrors, which measures the SHG intensity at a fixed time delay with respect to the pump. The probe fluence was fixed to $1.5\ \text{mJ}/\text{cm}^2$. A complete instantaneous SHG-RA pattern is acquired by mechanically co-rotating the input polarizer, phase mask, and output polarizer, which implements a rotation of the probe scattering plane about the sample surface normal, and then projecting the SHG light reflected at each scattering plane angle onto different positions along a circular locus of points on the CCD camera (see ref. 35 for further details). The procedure for converting raw CCD data to the polar SHG-RA plots shown in the main text is described in Supplementary Note 8. The SHG dynamics shown in Fig. 3 were reproduced under different polarization geometries and different scattering plane angles as shown in Supplementary Note 9.

Time-resolved linear reflectivity. Transient reflectivity measurements were performed using exactly the same setup as that used for time-resolved SHG-RA as described above. Identical experimental conditions were preserved for the reflectivity and SHG-RA measurements, with the only change between experimental runs being the spectral filtering optics before the CCD camera to either isolate the 800 nm or 400 nm output.

Time-resolved MOKE. Experiments were performed by splitting light from a regeneratively amplified Ti:sapphire laser (repetition rate 1 kHz; pulse energy 6 mJ; pulse duration 100 fs; central wavelength $\lambda = 800$ nm) into pump and probe arms. The pump arm feeds a collinear dual-stage optical parametric amplifier, whose 1300 nm output beam is circularly polarized and then focused onto the sample at normal incidence ($F = 4.6\ \text{mJ}/\text{cm}^2$). The probe arm ($\lambda = 800$ nm) is linearly S-polarized and focused near normal incidence onto the sample. To measure the polarization rotation (Kerr) angle of the reflected probe light, the reflected probe beam is sent through a half-wave plate followed by a Wollaston prism. These optics are oriented such that in the absence of a pump beam ($\theta_k = 0$), two equally intense beams of orthogonal linear polarization are produced, which are fed into the two input channels of a balanced photo-detector.

Conversion from F to n_{ex} . The number of photo-excitations n_{ex} created by the pump beam was calculated using the following equation:

$$n_{\text{ex}} = \frac{F(1-R)V_{\text{uc}}}{N_{\text{Ir}}E_{\text{ph}}\delta} \quad (2)$$

where F is the pump fluence, $R = 0.2$ and $\delta = 100$ nm are the sample reflectivity and penetration depth respectively at the pump wavelength $\lambda = 1400$ nm^{36,37}, V_{uc} .

is the unit cell volume of Sr_2IrO_4 , N_{Ir} is the number of Ir atoms per unit cell, and E_{ph} the pump photon energy (0.89 eV).

Exponential fitting procedure for linear reflectivity. Transient linear reflectivity curves were fit to a double exponential function of the form $\Delta R/R = Ae^{-t/\tau_0} + Be^{-t/\tau_1} + C$. A high quality of fit is achieved as shown in Fig. 4a. The timescales extracted for τ_0 (≈ 1 ps) and τ_1 (≈ 200 fs) agree with the two exponential timescales associated with the decay of photo-induced midgap states observed by ultrafast angle-resolved photoemission spectroscopy measurements²³, attributed to acoustic phonon and optical phonon mediated photo-carrier relaxation processes respectively. Since the rate-limiting step for photo-carrier relaxation is τ_0 , that is what we plot in the inset of Fig. 4a. We note that ref. ²³, also reported an absence of any fluence dependence for τ_0 , which is consistent with our observations (inset Fig. 4a).

Data availability

All relevant data presented in this paper are available from the corresponding author upon reasonable request.

Received: 23 November 2021; Accepted: 19 January 2022;

Published online: 04 February 2022

References

- Werner, P., Tsuji, N. & Eckstein, M. Nonthermal symmetry-broken states in the strongly interacting Hubbard model. *Phys. Rev. B* **86**, 205101 (2012).
- Sandri, M. & Fabrizio, M. Nonequilibrium dynamics in the antiferromagnetic Hubbard model. *Phys. Rev. B* **88**, 165113 (2013).
- Tsuji, N., Eckstein, M. & Werner, P. Nonthermal antiferromagnetic order and nonequilibrium criticality in the Hubbard Model. *Phys. Rev. Lett.* **110**, 136404 (2013).
- Walldorf, N., Kennes, D. M., Paaske, J. & Millis, A. J. The antiferromagnetic phase of the Floquet-driven Hubbard model. *Phys. Rev. B* **100**, 121110(R) (2019).
- Kim, B. J. et al. Novel $J_{\text{eff}} = 1/2$ Mott state Induced by relativistic spin-orbit coupling in Sr_2IrO_4 . *Phys. Rev. Lett.* **101**, 076402 (2008).
- Fujiyama, S. et al. Two-dimensional Heisenberg behavior of $J_{\text{eff}} = 1/2$ isospins in the paramagnetic state of the spin-orbital Mott insulator Sr_2IrO_4 . *Phys. Rev. Lett.* **108**, 247212 (2012).
- Vale, J. G. et al. Importance of XY anisotropy in Sr_2IrO_4 revealed by magnetic critical scattering experiments. *Phys. Rev. B* **92**, 020406 (2015).
- Porras, J. et al. Pseudospin-lattice coupling in the spin-orbit Mott insulator Sr_2IrO_4 . *Phys. Rev. B* **99**, 085125 (2019).
- Chen, X. et al. Influence of electron doping on the ground state of $(\text{Sr}_{1-x}\text{La}_x)_2\text{IrO}_4$. *Phys. Rev. B* **92**, 075125 (2015).
- Gretarsson, H. et al. Persistent paramagnons deep in the metallic phase of $\text{Sr}_{2-x}\text{La}_x\text{IrO}_4$. *Phys. Rev. Lett.* **117**, 107001 (2016).
- Pincini, D. et al. Anisotropic exchange and spin-wave damping in pure and electron-doped Sr_2IrO_4 . *Phys. Rev. B* **96**, 075162 (2017).
- Dean, M. P. M. et al. Ultrafast energy- and momentum-resolved dynamics of magnetic correlations in the photo-doped Mott insulator Sr_2IrO_4 . *Nat. Mater.* **15**, 601–605 (2016).
- Krupin, O. et al. Ultrafast dynamics of localized magnetic moments in the unconventional Mott insulator Sr_2IrO_4 . *J. Phys. Condens. Matter* **28**, 32LT01 (2016).
- Afanasiev, D. et al. Ultrafast spin dynamics in photodoped spin-orbit Mott insulator Sr_2IrO_4 . *Phys. Rev. X* **9**, 021020 (2019).
- Mazzzone, D. G. et al. Laser-induced transient magnons in $\text{Sr}_3\text{Ir}_2\text{O}_7$ throughout the Brillouin zone. *Proc. Nat. Acad. Sci. USA* <https://doi.org/10.1073/pnas.2103696118> (2021).
- Pastor, E. et al. Non-thermal breaking of magnetic order via photo-generated spin defects. *Phys. Rev. B* Preprint at <http://arxiv.org/abs/2104.04294> [cond-mat.str-el]. (2021).
- DiMatteo, S. & Norman, M. R. Magnetic ground state of Sr_2IrO_4 and implications for second-harmonic generation. *Phys. Rev. B* **94**, 075148 (2016).
- Seyler, K. L. et al. Spin-orbit-enhanced magnetic surface second-harmonic generation in Sr_2IrO_4 . *Phys. Rev. B* **102**, 201113 (R) (2020).
- Jeong, J., Sidis, Y., Louat, A., Brouet, V. & Bourges, P. Time-reversal symmetry breaking hidden order in $\text{Sr}_2(\text{Ir,Rh})\text{O}_4$. *Nat. Commun.* **8**, 15119 (2017).
- Murayama, H. et al. Bond directional anapole order in a spin-orbit coupled Mott insulator $\text{Sr}_2(\text{Ir}_{1-x}\text{Rh}_x)\text{O}_4$. *Phys. Rev. X* **11**, 011021 (2021).
- Zhao, L. et al. Evidence of an odd-parity hidden order in a spin-orbit coupled correlated iridate. *Nat. Phys.* **12**, 32–36 (2016).
- Takahashi, A., Gomi, H. & Aihara, M. Photoinduced superconducting states in strongly correlated electron systems. *Phys. Rev. B* **66**, 115103 (2002).
- Piovera, C. et al. Time-resolved photoemission of Sr_2IrO_4 . *Phys. Rev. B* **93**, 241114 (2016).
- Battisti, I. et al. Universality of pseudogap and emergent order in lightly doped Mott insulators. *Nat. Phys.* **13**, 21–25 (2017).
- Hsieh, D., Mahmood, F., Torchinsky, D. H., Cao, G. & Gedik, N. Observation of a metal-to-insulator transition with both Mott-Hubbard and Slater characteristics in Sr_2IrO_4 from time-resolved photocarrier dynamics. *Phys. Rev. B* **86**, 035128 (2012).
- Gim, Y. et al. Isotropic and anisotropic regimes of the field-dependent spin dynamics in Sr_2IrO_4 : Raman scattering studies. *Phys. Rev. B* **93**, 024405 (2016).
- Gretarsson, H. et al. Raman scattering study of vibrational and magnetic excitations in $\text{Sr}_{2-x}\text{La}_x\text{IrO}_4$. *Phys. Rev. B* **96**, 115138 (2017).
- Seifert, U. F. P. & Balents, L. Optical excitation of magnons in an easy-plane antiferromagnet: application to Sr_2IrO_4 . *Phys. Rev. B* **100**, 125161 (2019).
- Tengdin, P. et al. Critical behavior within 20 fs drives the out-of-equilibrium laser-induced magnetic phase transition in nickel. *Sci. Adv.* <https://doi.org/10.1126/sciadv.aap9744> (2018).
- Zong, A. et al. Dynamical slowing-down in an ultrafast photoinduced phase transition. *Phys. Rev. Lett.* **123**, 097601 (2019).
- de la Torre, A. et al. Collapse of the Mott gap and emergence of a nodal liquid in lightly doped Sr_2IrO_4 . *Phys. Rev. Lett.* **115**, 176402 (2015).
- Hohenberg, P. C. & Halperin, B. I. Theory of dynamic critical phenomena. *Rev. Mod. Phys.* **49**, 435–479 (1977).
- Sieberer, L. M., Buchhold, M. & Diehl, S. Keldysh field theory for driven open quantum systems. *Rep. Prog. Phys.* **79**, 096001 (2016).
- Dolgirev, P. E., Michael, M. H., Zong, A., Gedik, N. & Demler, E. Self-similar dynamics of order parameter fluctuations in pump-probe experiments. *Phys. Rev. B* **101**, 174306 (2020).
- Harter, J. W., Niu, L., Woss, A. J. & Hsieh, D. High-speed measurement of rotational anisotropy nonlinear optical harmonic generation using position-sensitive detection. *Opt. Lett.* **40**, 4671–4674 (2015).
- Lee, J. S., Krockenberger, Y., Takahashi, K. S., Kawasaki, M. & Tokura, Y. Insulator-metal transition driven by change of doping and spin-orbit interaction in Sr_2IrO_4 . *Phys. Rev. B* **85**, 035101 (2012).
- Nichols, J. et al. Anisotropic electronic properties of a-axis-oriented Sr_2IrO_4 epitaxial thin-films. *Appl. Phys. Lett.* **103**, 131910 (2013).

Acknowledgements

We thank L. Balents, A. Cavalleri, S. K. Cushing, E. Demler, S. Di Matteo, M. Endres, B. Fine, N. Gedik, D. Kennes, O. Mehio, H. Ning, M. Norman, and M. Sentef for useful discussions. This work is supported by ARO MURI Grant No. W911NF-16-1-0361. D.H. also acknowledges support for instrumentation from the David and Lucile Packard Foundation and from the Institute for Quantum Information and Matter (IQIM), an NSF Physics Frontiers Center (PHY-1733907). A.d.I.T. acknowledges support from the Swiss National Science Foundation through an Early Postdoc Mobility Fellowship (P2GEP2_65044). M.B. acknowledges support from the Alexander von Humboldt foundation. N.J.L. acknowledges support from an IQIM Fellowship. G.C. acknowledges NSF support via a grant DMR-1712101.

Author contributions

X.C., S.D.W., and G.C. synthesized and characterized the Sr_2IrO_4 crystals. A.d.I.T., K.L.S., and I.P. performed the SHG-RA measurements. J.W.H., L.Z., and A.d.I.T. built the SHG-RA apparatus. G.Z. and R.D.A. performed the MOKE measurements. M.B., Y.B., and G.R. performed the Langevin theory calculations. A.d.I.T., N.J.L., and D.H. analyzed the data. A.d.I.T. and D.H. wrote the paper with input from all authors.

Competing interests

The authors declare no competing interests.

Additional information

Supplementary information The online version contains supplementary material available at <https://doi.org/10.1038/s42005-022-00813-6>.

Correspondence and requests for materials should be addressed to David Hsieh.

Peer review information *Communications Physics* thanks the anonymous reviewers for their contribution to the peer review of this work.

Reprints and permission information is available at <http://www.nature.com/reprints>

Publisher's note Springer Nature remains neutral with regard to jurisdictional claims in published maps and institutional affiliations.



Open Access This article is licensed under a Creative Commons Attribution 4.0 International License, which permits use, sharing, adaptation, distribution and reproduction in any medium or format, as long as you give appropriate credit to the original author(s) and the source, provide a link to the Creative Commons license, and indicate if changes were made. The images or other third party material in this article are included in the article's Creative Commons license, unless indicated otherwise in a credit line to the material. If material is not included in the article's Creative Commons license and your intended use is not permitted by statutory regulation or exceeds the permitted use, you will need to obtain permission directly from the copyright holder. To view a copy of this license, visit <http://creativecommons.org/licenses/by/4.0/>.

© The Author(s) 2022